Morphology of long gas bubbles propagating in square capillaries

M. Magnini[1*], O. K. Matar[2]

[1] *Department of Mechanical, Materials and Manufacturing Engineering, University of Nottingham, Nottingham NG7 2RD, United Kingdom*

[2] *Department of Chemical Engineering, Imperial College London, London SW7 2AZ, United Kingdom*

Abstract

We present the results of a systematic analysis of the morphology of the thin lubrication film surrounding a long gas bubble transported by a liquid flow in a square capillary. Direct numerical simulations of the flow are performed using the Volume-Of-Fluid method implemented in OpenFOAM, for a range of capillary and Reynolds numbers $\mathrm{Ca} = 0.002 - 0.5$ and $\mathrm{Re} = 1 - 2000$, and very long bubbles, up to 20 times the hydraulic diameter of the channel. The lubrication film surrounding the bubbles is always resolved by the computational mesh, and therefore the results are representative of a fully-wetting liquid. This study shows that when $\mathrm{Ca} \geq 0.05$, the long gas bubble exhibits an axisymmetric shape on the channel cross-section, whereas for lower capillary numbers the bubble flattens at the centre of the channel wall and thick liquid lobes are left at the corners. When $\mathrm{Ca} \leq 0.01$, the thin film at the centre of the wall assumes a saddle-like shape, which leads to the formation of two constrictions at the sides of the liquid film

*Corresponding author. E-mail: mirco.magnini@nottingham.ac.uk

profile, where minimum cross-sectional values of the film thickness are observed. The resulting cross-stream capillary pressure gradients drain liquid out of the thin-film, whose thickness decreases indefinitely as a power-law of the distance from the bubble nose. Therefore, the film thickness depends on the length of the bubble, unlike flow in circular channels. We report detailed values of the centreline, diagonal and minimum film thickness along the bubble, bubble speed, and cross-sectional gas area fraction, at varying Ca and Re. Inertial effects retard the formation of the saddle-shaped thin-film at the channel centre, which may never form if the bubble is not sufficiently long. However, the film thins at a faster rate towards the bubble rear as the Reynolds number of the flow is increased.
Keywords: Bubbles, Surface tension, Microchannel, Two-Phase, Volume-Of-Fluid, Thin film

---

1. Introduction

The dynamics of thin liquid film flows and their gas-liquid interfaces in micro-geometries is key to many diverse processes and applications that span different disciplines, ranging from mechanical and environmental engineering to biological and medical science, such as microchannel two-phase cooling [1], transport of pollutants in unsaturated soil [2], cleaning of bacterial cells from medical surfaces [3], medical therapy [4], simultaneous humidification and thermal management of fuel cells [5]. At the pore scale, the two-phase flow is idealised as a long gas bubble displacing a wetting liquid as it propagates within a rigid channel, and leaving a thin liquid film at the wall. The topology and thickness of the liquid film depend on the competition between viscous

and capillary forces, quantified by the capillary number $\mathrm{Ca} = \mu_l U/\sigma$ (with μ_l being the liquid dynamic viscosity, U the bubble or average liquid speed, and σ the surface tension), by the competition of inertial and viscous forces, characterised by the Reynolds number $\mathrm{Re} = \rho_l U L/\mu_l$ (where ρ_l is the liquid density and L a characteristic length of the channel cross-section), and by a parameter reflecting the cross-sectional shape of the channel, e.g. the aspect-ratio in rectangular channels [6]. The problem has been studied extensively for flow in circular capillaries, starting with the seminal works of Bretherton [7] and Taylor [8]. In circular tubes, a flat film region develops sufficiently far from the nose and rear menisci of the bubble. The film thickness h in the flat film region is known to scale as $h \sim \mathrm{Ca}^{2/3}$ when $\mathrm{Ca} \leq 0.005$ and $\mathrm{Re} \ll 1$ [7]; the correction $h \sim \mathrm{Ca}^{2/3}/(1+\mathrm{Ca}^{2/3})$ is necessary to extend the validity of the correlation to capillary numbers up to $\mathrm{Ca} = 2$ [9]; inertial effects ($\mathrm{Re} \gg 1$) are implemented by introducing a correction term dependent on the Reynolds number at the denominator [9, 10]. Furthermore, fully-theoretical models based on the lubrication approximation are available to predict the entire bubble profile [11, 12], from the nose all the way to the rear meniscus.

Capillaries with angular cross-sections are expected to better represent the tortuosity of the gaps within porous media, or the shape of channels in microfluidic devices. When considering noncircular capillaries, the literature is still rather vast, although studies have mostly focused on the inertialess regime, where the Weber number of the flow, $\mathrm{We} = \mathrm{Ca}\,\mathrm{Re}$, is much smaller than unity. The first systematic analyses addressing the transport of bubbles in square channels can be attributed to Ratulowski and Chang [13] and Kolb and Cerro [14, 15], who found that below a threshold value of the

capillary number, Ca $= 0.04 - 0.1$, the cross-sectional shape of the bubble becomes non-axisymmetric, with a very thin liquid film at the channel centre and thick liquid lobes at the corners. Wong et al. [16, 17] developed an asymptotic analysis of the flow in the thin-film surrounding a long bubble advancing in a polygonal channel at quasi-static conditions. Their analysis revealed that surface tension forces rearrange the thin-film at the channel centre into a saddle profile, with a thickness of order $\mathrm{Ca}^{2/3}$ at the centre and order Ca^{1} at the sides where the film is the thinnest, and that the film thins indefinitely towards the bubble rear. Hazel and Heil [18] performed systematic simulations of the propagation of air fingers within noncircular channels for a wide range of capillary numbers (but $\mathrm{Re} \ll 1$) and confirmed that the cross-sectional profile of the finger becomes non-axisymmetric in square tubes when $\mathrm{Ca} \leq 0.04$. In this regime, they showed that a very thin film of liquid forms at the channel centre and the Laplacian pressure gradients arising between the channel centre and corners generate transversal flows that drive fluid flow into the corners. These results were later extended to rectangular channels by de Lózar et al. [6, 19], who provided scaling analyses to predict the wet area fraction (fraction of the channel cross-section occupied by the liquid) as a function of capillary number and channel aspect-ratio. More recently, Chen et al. [20, 21] measured the entire 3D profile of the lubrication film around long bubbles travelling in square microchannels by using a chromatic interference method. They investigated the range $\mathrm{Ca} \leq 0.01$ and $\mathrm{Re} \ll 1$ and confirmed the theoretical predictions of Wong et al. [16] that the minimum film thickness at the sides obeys $h_{min} \sim \mathrm{Ca}^{1}$ at short distance from the bubble nose, with the exponent gradually increasing to the asymptotic

value 4/3 as the distance is increased. Khodaparast et al. [22] proved that the sites of the local minima in the film thickness are critical locations for the stability of the film of partially-wetting liquids, which may eventually rupture and lead to the formation of dry patches.

The literature survey presented above reveals that a systematic analysis of the topological features of long bubbles travelling in noncircular channels for a wide range of capillary and Reynolds numbers is still missing. Essential information about the detailed perimetral distribution of the liquid film on the channel cross-section, the minimum and maximum values of the film thickness around the channel perimeter, the evolution of the film profile along the bubble, and how these features vary depending on the flow conditions, are still elusive despite being of great interest for the design and optimisation of two-phase microfluidic devices.

This work presents a thorough systematic analysis of the distinctive topological features characterising long gas bubbles propagating in square capillaries, for a wide range of capillary and Reynolds numbers, $\mathrm{Ca} = 0.002 - 0.5$ and $\mathrm{Re} = 1 - 2000$. Direct numerical simulations of the two-phase flow are performed utilising the Volume-Of-Fluid (VOF) method [23] implemented in OpenFOAM. This study emphasises that the dynamics of elongated bubbles in square channels, and the thickness of the resulting liquid films, differ substantially from those reported for circular channels. Depending on the capillary number of the flow, profoundly different shapes of the thin liquid film are observed. The length of the bubble and the inertial forces, that become relevant when $\mathrm{Re} \geq 100 - 500$, are key parameters influencing the topology of the gas-liquid interface. The rest of this article is organised as

follows: in Section 2, the numerical model is briefly introduced; in Section 3, a description of the flow problem is presented; Section 4 outlines the results of the systematic analysis; conclusions are summarised in Section 5.

2. Numerical method

Direct numerical simulations of the flow of elongated bubbles in square capillaries are performed utilising the VOF method [23] implemented in the interFoam solver of OpenFOAM. Accordingly, gas and liquid phases are treated as a single mixture fluid with variable properties across the interface, and a volume fraction field α is defined to map the phases throughout the flow domain. In each computational cell of the domain, α identifies the fraction of the cell volume occupied by the primary phase, which corresponds to gas in the present case. Therefore, the volume fraction takes values of 1 in the gas, 0 in the liquid, and $0 < \alpha < 1$ in cells that are intersected by the interface. By means of the volume fraction field, the properties of the mixture fluid can be computed as an average over the two phases, e.g. the density ρ:

$$\rho = \alpha\rho_g + (1 - \alpha)\rho_l \tag{1}$$

where the subscripts g and l denote gas- and liquid-specific properties, respectively.

The advantage of the single-fluid formulation is that a single set of conservation equations holds for both phases, which share a unique velocity and pressure field. We consider the incompressible and laminar flow of two Newtonian fluids, for which the governing equations of mass and momentum are

expressed as follows:

$$\nabla \cdot \mathbf{u} = 0 \tag{2}$$

$$\frac{\partial(\rho \mathbf{u})}{\partial t} + \nabla \cdot (\rho \mathbf{u}\mathbf{u}) = -\nabla p + \nabla \cdot \mu \left[(\nabla \mathbf{u}) + (\nabla \mathbf{u})^T \right] + \mathbf{F}_\sigma \tag{3}$$

where $\mathbf{u}$ indicates the fluid velocity, t the time, p the pressure, μ the dynamic viscosity, $\mathbf{F}_\sigma$ the surface tension force vector. All the fluid-specific properties, ρ_g, ρ_l, μ_g, and μ_l, are considered constant in this work. The surface tension force is formulated according to the Continuum Surface Force method [24] and computed as $\mathbf{F}_\sigma = \sigma\kappa|\nabla\alpha|$, where σ is the surface tension coefficient (considered constant) and κ the local interface curvature. The latter is estimated by means of derivatives of the volume fraction field, $\kappa = \nabla \cdot (\nabla\alpha/|\nabla\alpha|)$.

The mathematical problem is closed by a transport equation for the volume fraction, which allows the numerical model to update the location of the interface, and therefore the mixture fluid properties, as the two-phase flow evolves across the computational mesh:

$$\frac{\partial \alpha}{\partial t} + \nabla \cdot (\alpha \mathbf{u}) + \nabla \cdot [\alpha(1-\alpha)\mathbf{U_r}] = 0 \tag{4}$$

where $\mathbf{U_r}$ is an artificial compression velocity [25] and it is given by:

$$\mathbf{U_r} = \min \left[C_\alpha \frac{|\phi|}{|\mathbf{S_f}|}, \left(\frac{|\phi|}{|\mathbf{S_f}|} \right)_{\max} \right] \mathbf{n_f} \tag{5}$$

In Eq. (5), ϕ is the volumetric flux through the control volume face, $\mathbf{S_f}$ is the surface area vector of the cell face and $\mathbf{n_f}$ is the unit normal vector to the interface evaluated at the control volume face. C_α is a numerical parameter that tunes the interface compression, with $C_\alpha = 0$ indicating no compression, while increasing values enhance compression and thus lead to a sharper

interface. In the present work, the default value $C_\alpha = 1$ has been retained [26, 27, 28], as it ensured a good compromise between interface sharpness and accuracy in surface tension calculation.

OpenFOAM's VOF-based solver interFoam discretises the transport equations above with a finite-volume method, on a collocated grid arrangement. The volume fraction Eq. (4) is discretised with a first-order time-explicit scheme based on the MULES (Multidimensional Universal Limiter for Explicit Solution) algorithm [25], whereas the remaining equations are integrated in time with a first-order implicit scheme. The divergence operators are discretised using second-order TVD (Total Variation Diminishing) schemes [29], whereas Laplacian operators are discretised with central finite-differences. The PISO (Pressure Implicit Splitting of Operators) algorithm [30] is utilised to iteratively update pressures and velocities (3 corrections set) within each time-step. The residuals thresholds for the iterative solution of the flow equations are set to 10^{-7} for the velocity and 10^{-8} for both volume fraction and pressure. The time-step of the simulation is variable and is calculated based on a maximum allowed Courant number of 0.5.

3. Problem definition and simulation setup

We consider a long gas bubble propagating in a straight channel of square cross-section, with hydraulic diameter D_h (radius R_h), filled with a wetting Newtonian liquid; a schematic of the flow configuration under consideration is provided in Fig. 1. In order to describe the flow, we adopt a Cartesian reference frame where z denotes the streamwise coordinate, x the horizontal

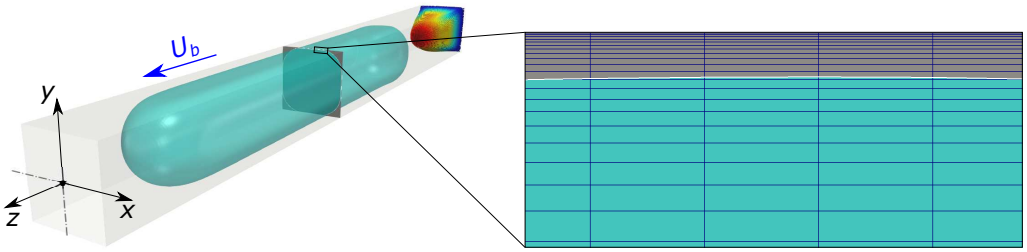

Figure 1: Illustration of the flow configuration under consideration ($\mathrm{Ca_l} = 0.005$, $\mathrm{Re_l} = 10$). An elongated gas bubble travels steadily at a speed U_b within a capillary channel of square cross-section, pushed by a fully-developed laminar flow of liquid. Under the conditions of interest, a thin film of liquid always wets the channel wall. The figure on the right shows a close-up look of the computational mesh on the channel cross-section, in the thin-film region ($h/R_h \approx 0.007$).

and y the vertical coordinate. The bubble moves steadily along z at a speed U_b, pushed by a laminar liquid flow of average velocity U_l. The no-slip condition applies at the channel wall, and therefore far from the bubble the liquid velocity profile is fully-developed. Gravity is neglected in this study and therefore the channel orientation is irrelevant. A thin film of liquid is trapped between the bubble and the channel wall, and the topology and thickness of this liquid film depends on the competition of viscous, capillary, and inertial forces. The relative importance of these forces is quantified by the capillary number $\mathrm{Ca} = \mu_l U/\sigma$ (viscous to capillary force) and by the Reynolds number $\mathrm{Re} = \rho_l U D_h/\mu_l$ (inertia to viscous force). Typically, in noncircular channels surface tension forces arrange the liquid in a thin-film region along the walls, with thick liquid lobes at the corners, as it can be observed in Fig. 1.

In the numerical model, the channel is modeled with a three-dimensional

geometry. At the inlet, a fully-developed laminar flow of liquid is set, together with a zero-gradient pressure condition. At the outlet, the pressure is set to a uniform reference value while a zero-gradient condition is applied to the velocity. No-slip is imposed at the channel walls. Owing to the $\pi/2$ symmetry of the flow, only one quarter of the cross-section is simulated and symmetry boundary conditions are utilised on the planes $x = 0$ and $y = 0$. A long gas bubble is initialised close to the channel inlet, its initial length L_b will be varied between $7D_h$ and $20D_h$ during the study. The liquid to gas density and viscosity ratios are set to 1000 and 100, respectively. The unsteady flow equations are solved in time until the bubble achieves a steady-state motion.

The range of capillary and Reynolds numbers studied in this work is $\mathrm{Ca_l} = 0.002 - 0.5$ and $\mathrm{Re_l} = 1 - 2000$, with U_l being used here as a velocity scale. The channel length in the simulation ranges from $20D_h$ for the low $\mathrm{Ca_l}$ range, to $100D_h$ for large $\mathrm{Ca_l}$ and $\mathrm{Re_l}$, due to the long distance that the bubble must travel before a steady propagation is observed. Very small thicknesses h of the thin liquid film are achieved, down to $h/R_h = 0.0025$ at the smallest capillary numbers studied. The thinnest film that can be adequately captured by the computational mesh depends on the size of the elements at the wall, with $5-10$ cells being necessary across the film to resolve the liquid velocity profile [31, 32]. We employ a structured mesh made of orthogonal hexahedra, with gradual refinement at the channel wall, as shown in Fig. 1. Following a mesh independence study, the finest mesh used for the smallest capillary numbers cases has the thinnest element next to the wall of thickness $2.9 \cdot 10^{-4} R_h$, with an expansion ratio of 1.16 in the wall-normal direction; this guarantees that at least $5 - 10$ cells discretise liquid films of

thicknesses $h/R_h = 0.002 - 0.006$ and above. For example, Fig. 1 shows the computational mesh in the thin-film region for a case run with $\mathrm{Ca_l} = 0.005$ and $\mathrm{Re_l} = 10$, where a thin-film of thickness $h/R_h \approx 0.007$ is discretised by 11 cells. Tests carried out with a finer mesh did not yield appreciable differences in the results (film thickness and bubble speed). Algebraic VOF methods such as MULES may lead to an artificial smearing of the liquid-gas interface. Under the present setup, the numerical thickness of the interface, measured as the number of cells whose volume fraction is between 0.01 and 0.99, is always of two computational cells. Tests performed with a finer mesh, where a thinner interface was achieved, did not yield appreciable differences, and therefore it can be concluded that the results are independent of the numerical thickness of the interface.

Overall, domain grids with number of cells ranging from 5 to 20 million were utilised, with longer channels requiring more computational resources. Simulations were run on a high-performance computing cluster, typically employing ten 12-core nodes (infiniband interconnection; available RAM: 40 GB per node) for each case, adopting OpenFOAM's scotch domain decomposition. The computational time for each simulation ranged from 3000 (low Re) to 20000 CPU hours (high Re).

As a validation test, we simulated the conditions analysed experimentally by Marschall et al. [33] for the flow of elongated bubbles in a vertical square channel, which was conducted for $\mathrm{Ca_b} = \mu_l U_b/\sigma = 0.088$ and $\mathrm{Re_b} = \rho_l U_b D_h/\mu_l = 17$, and thus within the range of interest of the present study. The deviation between the experimental and numerical values of the

film thickness is below 2%; details of the comparison are included in the Supplementary Material.

4. Results and discussion

A first series of numerical simulations was run by systematically varying the capillary number, but fixing the Reynolds number to a small value, $\mathrm{Re_l} \leq 10$, such that the Weber number of the flow $\mathrm{We_l} = \mathrm{Ca_l}\,\mathrm{Re_l} \ll 1$. This enables us to study in detail the visco-capillary regime, where the effects of inertial forces are expected to be negligible [9, 34]. The results for the negligible-inertia case are presented in Section 4.1. The visco-inertial regime was then investigated by systematically varying the Reynolds number, for selected values of the capillary number. The analysis of the impact of inertial forces on the bubble dynamics is provided in Section 4.2.

4.1. Flows with negligible inertia

4.1.1. Effect of the capillary number

In order to study the dynamics of long bubbles and thin liquid films in the negligible-inertia regime ($\mathrm{We} \ll 1$), we have performed numerical simulations by varying the capillary number in the range $\mathrm{Ca_l} = 0.002 - 0.5$, while fixing the Reynolds number to a small value. Figure 2(b) shows the cross-sectional radius of the bubble as a function of the capillary number, when the centreline ($y = 0$) and diagonal ($x = y$) radii are measured at a distance of $11R_h$ from the bubble tip, as indicated in Fig. 2(a). The choice of measuring the bubble radii at $11R_h$ and reporting these as a function of the bubble capillary number, $\mathrm{Ca_b} = \mu_l U_b/\sigma$, enables a direct comparison with

the results of the numerical study of Hazel and Heil [18]. As a general trend, the bubble radius decreases as the capillary number is increased and viscous forces overcome capillary forces, in agreement with the traditional thin-film theory [7]. Three different regimes for the topology of the liquid film, or cross-sectional shape of the bubble, are identified when varying $\mathrm{Ca_b}$. Above a certain threshold for the capillary number, $\mathrm{Ca_b} \geq 0.05$, centreline and diagonal bubble radii differ by less than 1% and the bubble is axisymmetric, as it can be observed in the cross-sectional profile of Fig. 2(c). This threshold

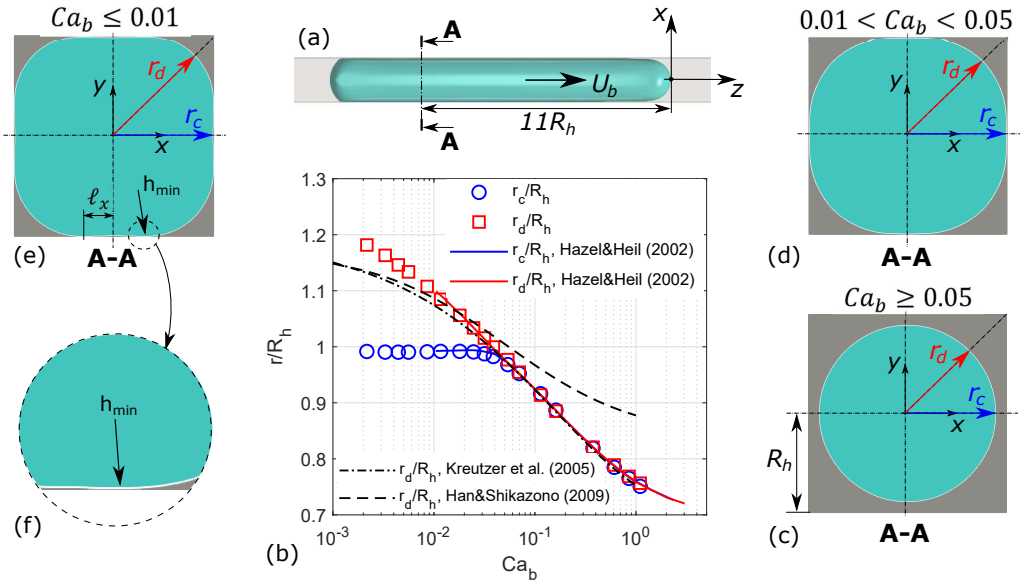

Figure 2: (a) Sketch of an elongated bubble travelling in a square capillary and (b) comparison of centreline and diagonal bubble radii, measured $11R_h$ behind the tip of the bubble nose, with Hazel and Heil [18] numerical study, and Han and Shikazono [35] and Kreutzer et al. [36] empirical correlations ($\mathrm{We_l} \ll 1$). (c), (d), (e) and (f) show representative cross-sectional bubble shapes at different regimes. In (e), ℓ_x denotes the cross-stream distance between the minimum film thickness location and the channel centre.

value agrees with the experimental measurements of Kolb and Cerro [14] and the theoretical predictions of Ratulowski and Chang [13]. For smaller capillary numbers, the two radii diverge because r_c is limited by the channel wall, such that $r_c \leq R_h$, whereas the diagonal radius can potentially grow up to $r_d = \sqrt{2}R_h$ if the liquid-gas interface reaches the channel corners. Figure 2(d) shows the non-axisymmetric bubble profile on the cross-section for this second regime, where the liquid film is the thinnest at the centre of the channel, while most of the liquid is pushed towards the corners. We identify a third regime which is encountered at smaller capillary numbers, and is characterised by the formation of a dimple on the interface between the channel centre and the corner, see Fig. 2(e) and (f), where the interface curvature changes sign and exhibits a saddle shape at the channel centre. The minimum film thickness value on the cross-section is detected in the vicinity of this dimple, at a distance from the channel centre indicated as ℓ_x. Our numerical simulations suggest that the dimple appears when $\mathrm{Ca_b} \leq 0.01$, in agreement with the observations of Ferrari et al. [37]. Further decrease of $\mathrm{Ca_b}$ in this regime does not yield appreciable differences in r_c, while r_d increases towards the asymptotic value of $r_d = 1.2R_h$ predicted by the theory of Wong et al. [16] for bubbles propagating in square channels at vanishing capillary numbers. The results of our numerical simulations agree remarkably well with those of Hazel and Heil [18], deviations for both r_c and r_d are below 1% across the entire range of $\mathrm{Ca_b}$ studied. For further comparison, Figure 2(b) includes also the predictions for the diagonal bubble radius obtained with two empirical correlations from the literature. The correlation of Kreutzer et al. [36] was obtained by fitting the numerical data of Hazel and Heil [18]

($0.01 \leq \mathrm{Ca_b} \leq 10$), the experimental data of Kolb and Cerro [14] for air bubbles in horizontal, upward and downward flow ($0.01 \leq \mathrm{Ca_b} \leq 10$), and the experimental data of Thulasidas et al. [38] for a train of bubbles rising in a vertical square channel ($10^{-4} \leq \mathrm{Ca_b} \leq 10$); it reads as follows:

$$\frac{r_d}{R_h} = 0.7 + 0.5 \exp^{-2.25\mathrm{Ca_b}^{0.445}} \tag{6}$$

Our numerical data compare very well with this correlation when $\mathrm{Ca_b} \geq 0.01$, while at lower capillary numbers the diagonal bubble radius in our simulations is about 5% larger. This can be ascribed to the fact that, when $\mathrm{Ca_b} < 0.01$, the empirical fit is based exclusively on the data of Thulasidas et al. [38]. These were obtained for air-water flow in a vertical channel of $D_h = 2\,\mathrm{mm}$, where gravitational forces induce an appreciable thickening effect on the liquid film already when the Bond number ($\mathrm{Bo} = \rho_l g R_h^2/\sigma$) is below 1 [39], thus explaining the underprediction of the numerical bubble radius observed in Fig. 2(b). The second correlation included in Fig. 2(b) was proposed by Han and Shikazono [35] and obtained by fitting their diagonal film thickness measurements for long air fingers displacing three different low-viscosity liquids (water, FC40 and ethanol), in $D_h = 0.3 - 1\,\mathrm{mm}$ horizontal square capillaries; for $\mathrm{We} \ll 1$, this reads as follows:

$$\frac{r_d}{R_h} = 1.171 - \frac{2.43\mathrm{Ca_b}^{2/3}}{1 + 7.28\mathrm{Ca_b}^{2/3}} \tag{7}$$

At large capillary numbers, Eq. (7) overestimates both our and Hazel and Heil [18] numerical data. Han and Shikazono [35] observed that their measurements could be either above or below Hazel and Heil [18] data at large capillary numbers, depending on the fluid and channel diameter. Deviations in this regime can be attributed to the effect of inertia, as $\mathrm{We} \gg 1$ in the

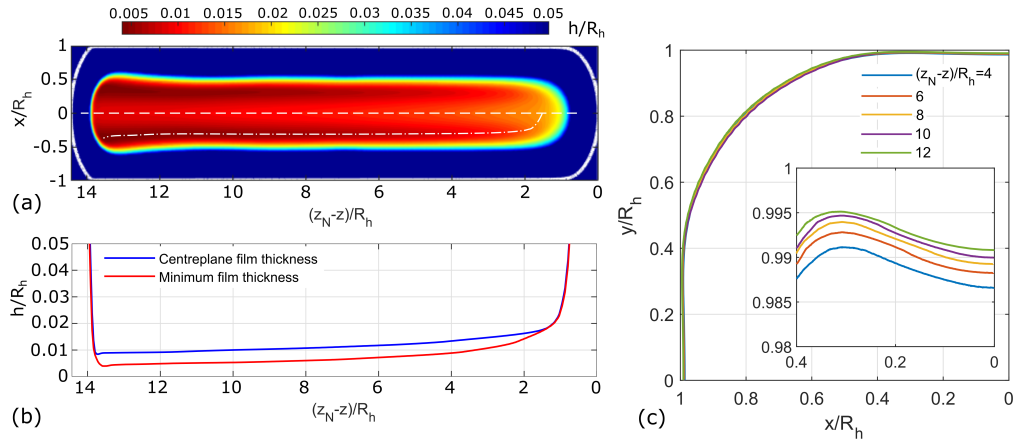

Figure 3: Topology of the elongated bubble and liquid film for $\mathrm{Ca_l} = 0.005$ ($\mathrm{We_l} \ll 1$): (a) contours of the liquid film thickness measured over the $y = R_h$ plane; (b) profiles of the streamwise film thickness extracted along the $x = 0$ axis (white dashed line in (a)) and along the minimum film thickness line (white dash-dot line in (a)); (c) cross-sectional ($x - y$ plane) liquid-gas interface profiles at different distance from the bubble nose, with the inset providing a close-up view near the centre of the wall. In (a) and (b), the bubble is moving from left to right; z_N indicates the streamwise coordinate of the bubble nose.

experiment due to the low-viscosity fluids employed. As $\mathrm{Ca_b}$ is reduced below 0.01, the predictions are slightly below the numerical data, due to the asymptotic value of 1.171 used in Eq. (7) for $\mathrm{Ca_b} \to 0$, which differs from the value of 1.2 obtained by Wong et al. [16], where our numerical results seem to converge.

4.1.2. Bubble shapes

In this section, representative profiles of the bubbles for the three regimes identified in the previous section are discussed. Figure 3 provides information about the liquid film distribution along the bubble for $\mathrm{Ca_l} = 0.005$, which be-

longs to the regime where the interface dimple appears. The contours of the film thickness in Fig. 3(a) reveal the formation of a minimum film thickness region that evolves towards the bubble rear, where the film becomes progressively thinner. In the cross-stream direction, the thinnest film is detected at a distance of $0.3R_h$ from the channel centreplane ($x = 0$), and the thin-film region occupies about half of the channel width, from $x/R_h \approx -0.5$ to 0.5. In Fig. 3(b), the liquid film thickness is extracted both along the channel centreline and along the minimum film thickness line. The two curves start to deviate at about $1.3R_h$ behind the bubble nose, where the dimple is first formed, and the thicknesses decrease monotonically until the rear meniscus, where the minimum thickness has become half the thickness on the centreline. Figure 3(c) illustrates the profiles of the liquid-gas interface at different cross-sections along the bubble, and suggests that the entire interface line in the thin-film region is shifting towards the wall, as cross-sections farther from the bubble front are considered. In the thin-film region, the interface curvature is positive (on the $x-y$ plane) and the liquid pressure is larger than that within the bubble because of the Laplace pressure jump ($p = p_b + \sigma\kappa$, with p_b being the bubble pressure), whereas at the corners the curvature is negative and thus the pressure is below that of the bubble. This transversal pressure gradient drives a transversal flow of liquid that drains the thin-film region, thus explaining the progressive thinning of the liquid film towards the bubble rear observed in Fig. 3(b). This aspect will be investigated in more detail in Section 4.1.4.

Figure 4 displays the topological features of the film surrounding the bubble for $\mathrm{Ca_l} = 0.02$, where the centreline bubble radius is still smaller than

that along the diagonal, but the interface dimple does no longer appear. In this regime, the minimum film thickness is detected along the channel centreline. The film thickness still decreases monotonically towards the bubble tail, and even at very large distances behind the bubble nose, see Fig. 4(c), the axial film thinning is still noticeable. Although the interface curvature has a constant sign all around the cross-sectional perimeter, the curvature change between the thin-film region and the channel corner is still significant, and hence draining flows still occur. It is interesting to note that the minimum film thickness at $28R_h$ behind the bubble tip has a similar value to the min-

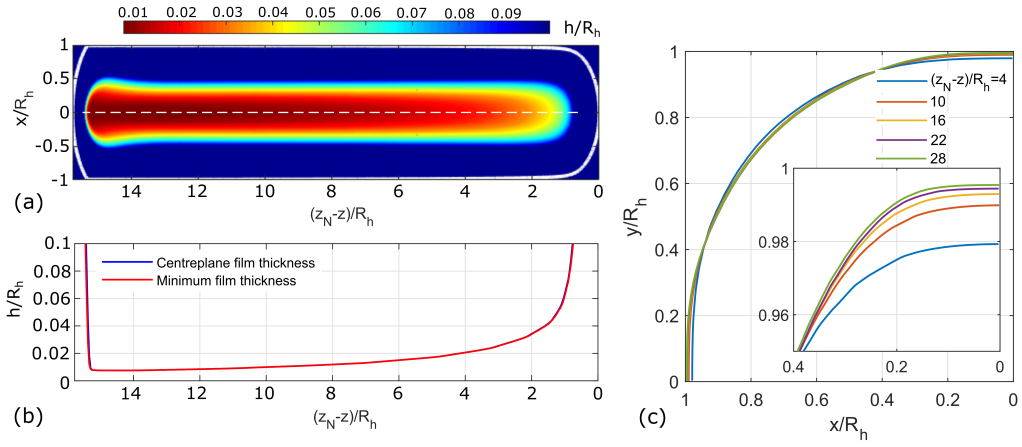

Figure 4: Topology of the elongated bubble and liquid film for $\mathrm{Ca_l} = 0.02$ ($\mathrm{We_l} \ll 1$): (a) contours of the liquid film thickness measured over the $y = R_h$ plane; (b) profile of the streamwise film thickness extracted along the $x = 0$ axis (white dashed line in (a)), which coincides with the minimum film thickness line; (c) cross-sectional ($x-y$ plane) liquid-gas interface profiles at different distance from the bubble nose, with the inset providing a close-up view near the centre of the wall. In (a) and (b), the bubble is moving from left to right; z_N indicates the streamwise coordinate of the bubble nose. In (c), the interface profiles are extracted from a case run with a longer bubble.

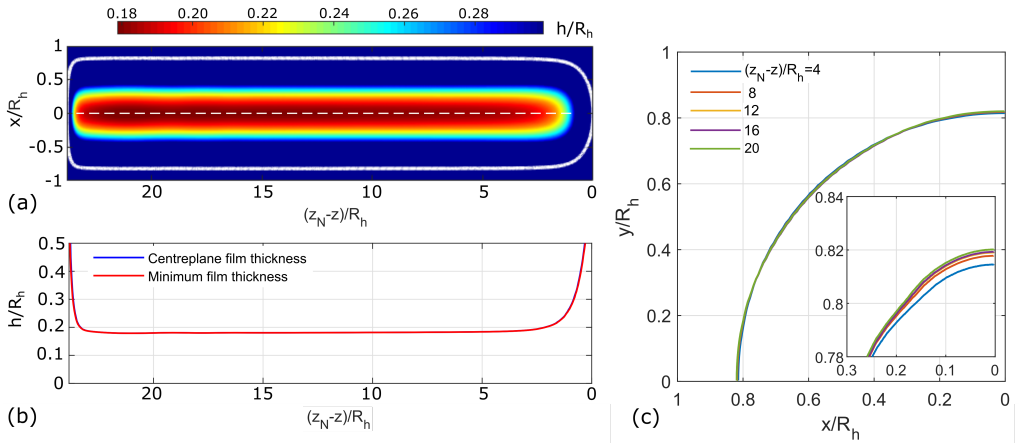

Figure 5: Topology of the elongated bubble and liquid film for $\mathrm{Ca_l} = 0.2$ ($\mathrm{We_l} \ll 1$): (a) contours of the liquid film thickness measured over the $y = R_h$ plane; (b) profile of the streamwise film thickness extracted along the $x = 0$ axis (white dashed line in (a)), which coincides with the minimum film thickness line; (c) cross-sectional ($x-y$ plane) liquid-gas interface profiles at different distance from the bubble nose, with the inset providing a close-up view near the centre of the wall. In (a) and (b), the bubble is moving from left to right; z_N indicates the streamwise coordinate of the bubble nose.

imum thickness measured for $\mathrm{Ca_l} = 0.005$ and $(z_N - z)/R_h = 12$ (Fig. 3(c)), despite the different concavity of the interface in the thin-film region. Once more, this emphasises the remarkable importance of the bubble length on the liquid film thickness in square channels. This differs substantially from the topology of long bubbles travelling in circular channels, where bubbles as short as $5R_h$ are sufficient for a flat film region to exist between the front and rear menisci, in the same conditions ($\mathrm{Ca_l} = 0.02$, $\mathrm{We} \ll 1$) [12].

Much thicker liquid films are detected for the case run with $\mathrm{Ca_l} = 0.2$, reported in Fig. 5. The bubble is axisymmetric and its body is exactly

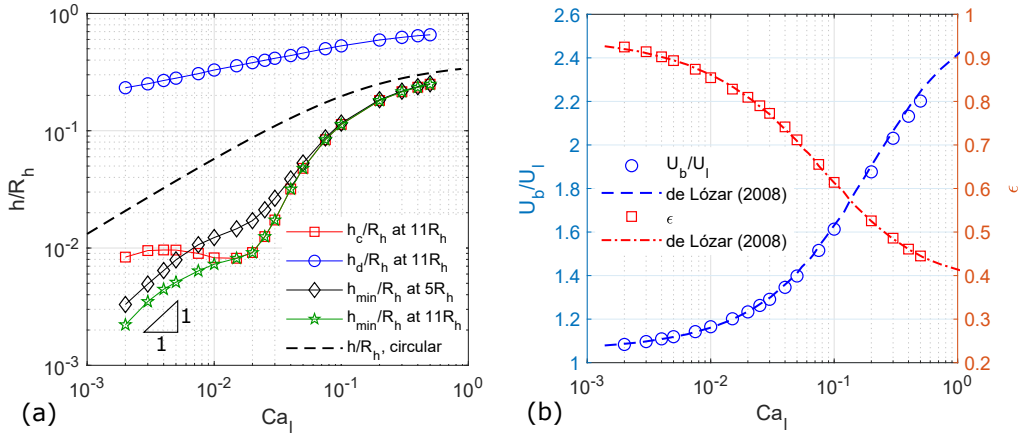

Figure 6: (a) Centreline, diagonal and minimum film thicknesses versus liquid capillary number ($We_l \ll 1$); the black dashed line indicates the film thickness prediction for a circular channel calculated using Aussillous and Quéré [9] correlation; (b) bubble-to-liquid velocity ratio and gas area fraction as a function of the liquid capillary number ($We_l \ll 1$); the dashed lines indicate the results of the numerical simulations of de Lózar et al. [19].

cylindrical. The change in the film thickness at the channel centre between $4R_h$ and $20R_h$ behind the bubble nose is less than 1%, thus suggesting that transversal flows are absent, so that the liquid pressure is uniform around the bubble.

4.1.3. Film thickness and bubble speed

This section focuses on flow parameters of interest for practical applications, such as the design of micro-evaporators or chemical reactors. Figure 6(a) displays the liquid film thickness along the cross-section diagonal, centreline, and the minimum thickness, evaluated at a given distance from the bubble tip, for all the Ca_l tested with the numerical simulations. The predictions extracted with the correlation of Aussillous and Quéré [9] for

circular channels are also included:

$$\frac{h}{R} = \frac{1.34\mathrm{Ca_b}^{2/3}}{1 + 3.35\mathrm{Ca_b}^{2/3}} \tag{8}$$

It can be seen that the diagonal film thickness h_d (evaluated as $h_d = \sqrt{2}R_h - r_d$) is considerably larger than the uniform thickness measured in circular channels, with an order of magnitude difference when $\mathrm{Ca_l} \leq 0.01$. On the other hand, the centreline film thickness h_c ($h_c = R_h - r_c$) is always below the value for circular channels, down to one order of magnitude smaller when $\mathrm{Ca_l} \leq 0.01$, so that $h_c \approx (1/100)h_d$ in this regime. Centreline and minimum film thicknesses match at large capillary numbers, until the interface dimple is formed and the two curves diverge when $\mathrm{Ca_l} \leq 0.01$. For decreasing values of $\mathrm{Ca_l}$, h_c first exhibits a slight increase due to the inversion of the thin-film curvature, and eventually it decreases monotonically as $\mathrm{Ca_l} \leq 0.004$. The asymptotic theory of Wong et al. [16] suggests that the centreline film thickness decreases as $h_c \sim \mathrm{Ca_b}^{2/3}$ when $\mathrm{Ca_b} \to 0$; the computational mesh presently employed does not allow to simulate values of $\mathrm{Ca_l}$ below 0.002, however the decreasing trend seems to be in qualitative agreement. The minimum film thickness h_{min} decreases monotonically as the capillary number is reduced (Fig. 6(a)); the simulation data yield an asymptotic scaling of $h_{min} \sim \mathrm{Ca_l}^1$ for $\mathrm{Ca_b} \to 0$, in perfect agreement with the theory of Wong et al. [16], who predicted the same power-law for the minimum film thickness occurring at a short distance from the bubble nose. Figure 6(a) also includes the minimum film thickness measured at $5R_h$ from the bubble tip; although the film is thicker than that measured at $11R_h$, the scaling $h_{min} \sim \mathrm{Ca_l}^1$ still holds at small $\mathrm{Ca_l}$.

The simulation results for the bubble-to-liquid velocity ratio and the gas

area fraction are presented in Fig. 6(b) as a function of the liquid capillary number. As a comparison, the figure also includes the results of the numerical simulations of de Lózar et al. [19], where the gas area fraction was extracted directly from the simulations and the velocity ratio is computed from the material liquid balance:

$$\frac{U_b}{U_l} = \frac{A}{A_b} = \frac{1}{\epsilon} \tag{9}$$

where A is the cross-sectional area of the channel, A_b is the area occupied by the bubble and ϵ the gas area fraction. Note that Eq. (9) is obtained under the assumption of negligible axial flow of liquid around the bubble. The agreement between de Lózar et al. [19] and our data is remarkable, thus suggesting that the stagnant liquid film assumption adopted to derive Eq. (9) holds well even at large capillary numbers. Wong et al. [16] theory predicts $U_b/U_l = 1.064$ and $\epsilon = 0.94$ as $\mathrm{Ca_b} \to 0$, which is in line with the data in Fig. 6(b).

4.1.4. Interface topology in the minimum film thickness region

In this section we provide a thorough analysis of the thin-film region in the presence of the interface dimple, thus focusing on conditions characterised by $\mathrm{Ca_l} \leq 0.01$. In this regime, the minimum film thickness h_{min} can become substantially smaller than the centreline thickness h_c, as observed in Fig. 6(a). On a generic channel cross-section, e.g. A-A in Fig. 2(a), the transversal distance between the minimum thickness location and the channel centre ($x = 0$ plane) is indicated as ℓ_x, see the schematic in Fig. 2(e). Since the thin-film occupies the region $0 \leq x \leq \ell_x$, the nondimensional parameter ℓ_x/R_h provides an estimation of the fraction of the cross-sectional perimeter covered by a thin film. Figure 7(a) plots ℓ_x/R_h as a function of the distance

from the bubble nose, for different values of the capillary number. At the bubble nose, the minimum film thickness is detected at the channel centre, so that $\ell_x = 0$. The dimple appears at a distance of $(1.2 - 1.8)R_h$ from the nose, where the minimum film thickness location shifts from the channel centre. From about $4R_h$ behind the bubble tip, ℓ_x is constant towards the bubble tail, as predicted by Wong et al. [16].

For each value of $\mathrm{Ca_l}$, we extract ℓ_x along the bubble body (where this is constant) and plot it in Fig. 7(b); in this figure, we also include the result of a simulation run with $\mathrm{Ca_l} = 0.001$, where the film eventually dewets due to insufficient mesh resolution. When $\mathrm{Ca_l} > 0.01$, the thinnest film is detected along the channel centreline. As the capillary number is reduced, the minimum thickness region shifts sideways and ℓ_x/R_h converges to the asymptotic value of 0.47 predicted by Wong et al. [16], i.e. almost half of the cross-sectional perimeter is covered by a very thin film.

Additional insight to the cross-sectional profile of the liquid-gas interface at varying $\mathrm{Ca_l}$ is provided with Fig. 7(c). Here, it is further observed that the interface dimple moves towards the channel corner as the capillary number decreases, and that the minimum film thickness decreases at a faster rate than that along the centreline. Due to the very thin films observed at the interface dimple, liquid film dryout is expected to initiate at the locations indicated in Fig. 7(b), as observed experimentally by Khodaparast et al. [22] and theoretically by Kreutzer et al. [40] for the adiabatic flow of long air bubbles in noncircular microchannels. If dryout does not occur, the thin film observed between $x = 0$ and $x = \ell_x$ is expected to be beneficial for applications such as flow boiling in microchannels [41] or bubble-driven detachment

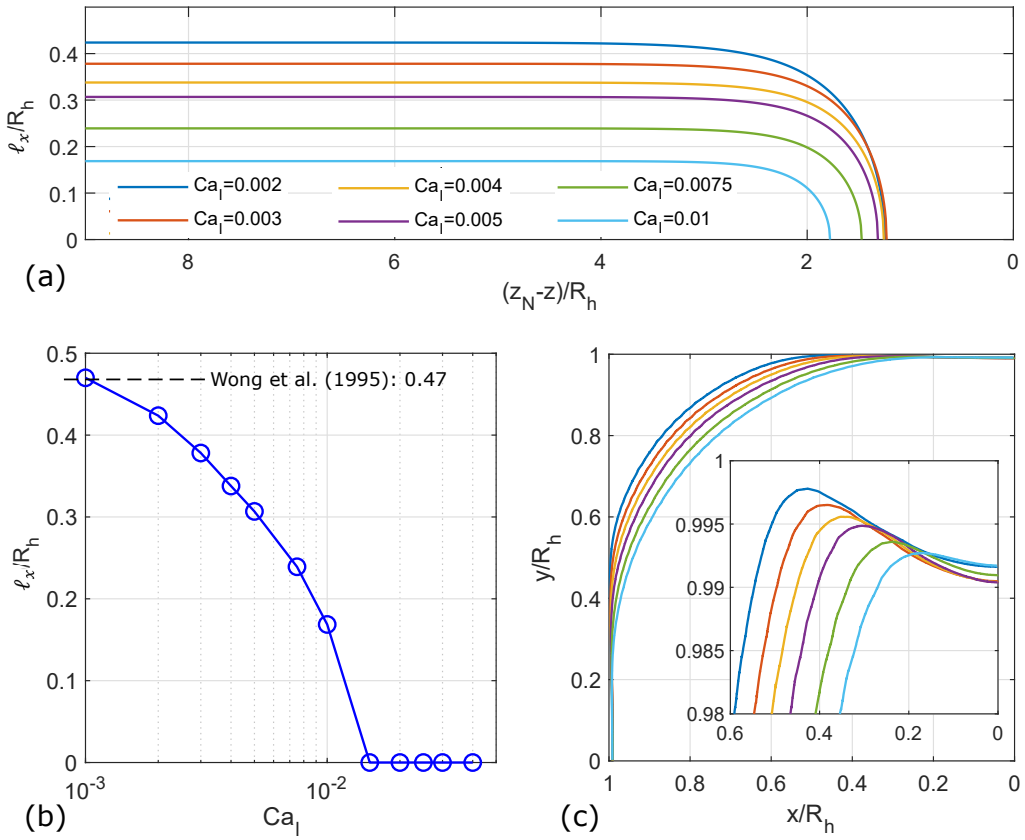

Figure 7: Analysis of the simulation results for the $\mathrm{Ca_l} \leq 0.01$ regime ($\mathrm{We_l} \ll 1$): (a) streamwise profiles of the distance ℓ_x between the minimum thickness location and the $x = 0$ plane (see the white dash-dot line in Fig. 3(a)); (b) distance between the minimum thickness location and the $x = 0$ plane as a function of the liquid capillary number; (c) cross-sectional liquid-gas interface profiles at different capillary numbers (the same colour legend as in (a) applies), extracted at $11R_h$ from the bubble nose.

of colloids from confined microgeometries [3, 2].

An interesting streamwise liquid film thinning trend emerges when plotting the minimum film thickness along the bubble (e.g. Fig. 3(b), red curve)

in logarithmic coordinates, see Fig. 8. Based on the observed trend, the bubble can be decomposed along its length into two distinct zones: the nose region at the bubble front tip, where $(z_N - z) < R_h$; and the bubble body behind it, $(z_N - z) > R_h$, where the dimple and the thin-film region at the channel centre have formed. In this latter region, the minimum film thickness decays as a linear function of the distance from the nose, thus suggesting a power-law dependence $h_{min} \sim (z_N - z)^{-\beta}$. The exponent β represents the slope of the streamwise film thickness profile in log-log coordinates. We extract the value of β for each $\mathrm{Ca_l}$ as the exponent that yields the best fit of the power-law to the $h_{min}(z)$ profile in the simulation, and obtain values in the range $\beta = 0.5 - 0.67$ for $\mathrm{Ca_l} = 0.002 - 0.01$, see the data in the inset of Fig. 8.

In order to provide physical grounds to the observed film thinning trend, we utilise an analytical model to describe the evolution of the liquid film in the thin-film region at the channel centre. The model is based on the solution of the Navier-Stokes equations for a flow with a free-surface, simplified under the lubrication approximation [42, 16, 34]. The full derivation is included in the Appendix; below, the main results are reported and compared with the simulation data. We adopt a reference frame analogous to that depicted in Fig. 1, where z denotes the streamwise coordinate, and $h(x, z)$ is a two-dimensional function that describes the height of the liquid film covering the channel wall, evaluated as the distance between the $y = R_h$ boundary and the liquid-gas interface. We consider the thin-film region between the dimple and the channel centre, where $0 \leq x \leq \ell_x$, and far from the bubble nose and tail. In this region, the thickness of the film is much smaller than its

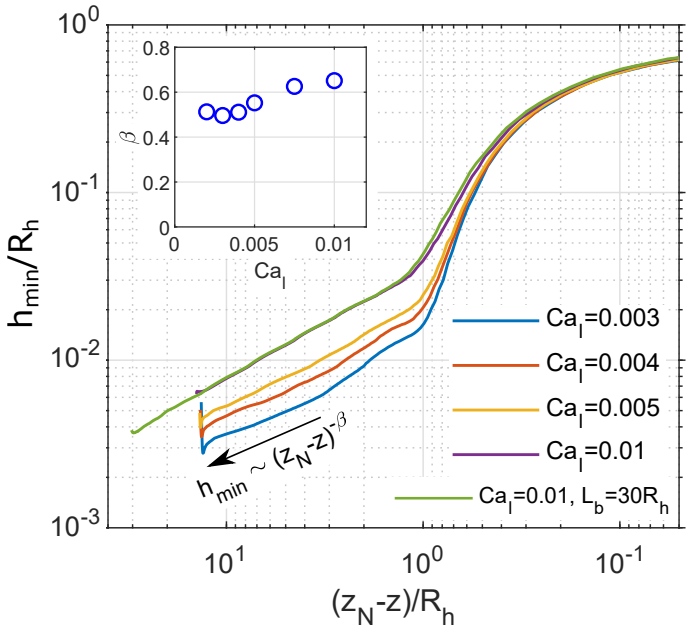

Figure 8: Streamwise profiles of the film thickness extracted along the minimum film thickness line, for different capillary numbers ($We_l \ll 1$), plotted in logarithmic axes; the inset reports the values of the slope of the film thickness lines, identified as the exponent β of the function $h_{min} \sim (z_N - z)^{-\beta}$ that best fits the simulation data in the rearmost region of the bubble, $(z_N - z)/R_h > 3$.

streamwise and cross-stream extension, $h \ll L_b$ and $h \ll \ell_x$, the film is nearly parallel to the wall, $|\nabla h| \ll 1$, and therefore the lubrication approximation applies. Accordingly, the fluid flow within the film is taken to be nearly parallel to the wall and the velocity field is described as a two-component vector $\mathbf{u}(x, y, z) = u(x, y, z)\mathbf{i} + w(x, y, z)\mathbf{k}$, where u is the component along x and w that along z.

The pressure in the film is independent of y, i.e. the pressure is constant along a direction perpendicular to the wall, and thus the pressure field can

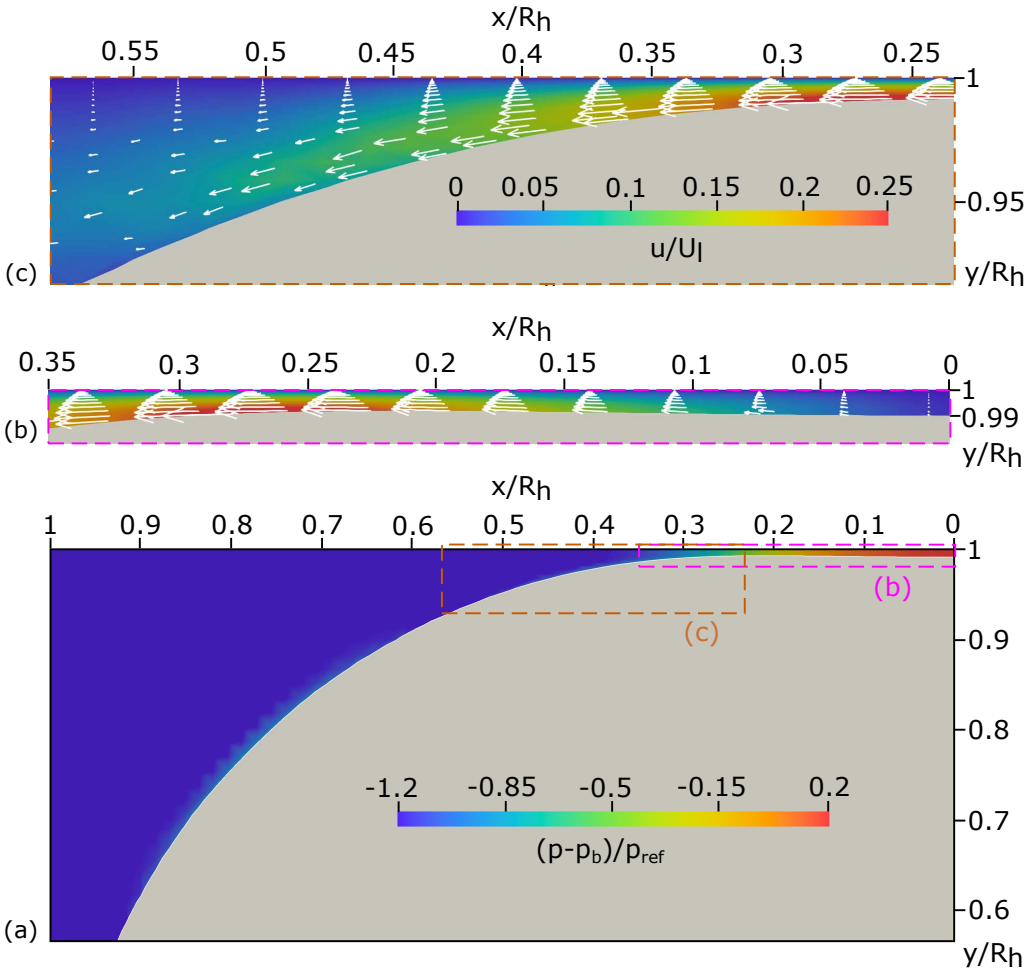

Figure 9: Cross-sectional pressure field and draining flows for $\mathrm{Ca_l} = 0.01$ ($\mathrm{We_l} \ll 1$). (a) Pressure field on a cross-section at a distance of $11R_h$ from the bubble nose; the region occupied by the bubble is coloured in grey; $p_{ref} = \sigma/R_h$ is used as a pressure scale. (b,c) Horizontal component of the velocity and velocity vectors in the thin-film region.

be described as a two-dimensional function:

$$p(x,z) = p_b + \sigma\kappa(x,z) = p_b - \sigma\nabla^2 h(x,z) \tag{10}$$

where p_b is the pressure inside the bubble (assumed constant) and $\kappa(x,z) =$

$-\nabla^2 h(x,z)$ is the local interface curvature; note that $\nabla^2 h < 0$ at the channel centre and $\nabla^2 h > 0$ at the corners. Figure 9(a) illustrates the pressure field on a selected cross-section for a simulation run with $\mathrm{Ca_l} = 0.01$. Near the channel centre, where $x < \ell_x$, the interface curvature is positive and $p > p_b$ in agreement with Eq. (10), whereas at the channel corner $p < p_b$. Equation (10) can be utilised to derive an expression for the pressure gradient:

$$\nabla p = -\sigma \nabla \left(\nabla^2 h \right) \tag{11}$$

where $\nabla = \mathbf{i}\,\partial/\partial x + \mathbf{k}\,\partial/\partial z$. The equation above indicates that the pressure gradient mobilising the liquid in the thin-film region is the capillary pressure gradient induced by changes of the interface curvature.

We consider a reference frame moving with the bubble at a speed $U_b\mathbf{k}$. In accordance with the no-slip condition, the wall moves with velocity $-U_b\mathbf{k}$ and the velocity profile in the liquid film can be expressed as:

$$\mathbf{u}(x,y,z) = -U_b\mathbf{k} + \frac{1}{\mu}\nabla p \left[\frac{1}{2}(R_h - y)^2 - h(R_h - y) \right] \tag{12}$$

where y varies between $y = R_h - h(x,z)$ at the bubble interface and $y = R_h$ at the channel wall. Equation (12) shows that, in a reference frame moving with the bubble, the fluid velocity in the film has two contributions. The first is due to the motion of the wall and has only an axial component ($-U_b\mathbf{k}$), whereas the second is due to the capillary pressure gradient and may have both streamwise and cross-stream components, depending on the interface profile. Figure 9(b) and (c) depicts the flow field in the thin-film region and reveals the occurrence of transversal flows driven by the cross-stream pressure gradient $\partial p/\partial x = -\sigma \partial \left(\nabla^2 h \right) / \partial x$. Note that $\partial \left(\nabla^2 h \right) / \partial x > 0$ in the thin-film, such that $\partial p/\partial x < 0$. The velocity magnitude of the transversal flows is

substantial, as it reaches values as high as $u \approx 0.25U_l$. We emphasise that, in a stationary reference frame, the cross-stream velocity component in the film in Fig. 9(b) and (c) is one order of magnitude larger than the streamwise component (not reported in the figure), thus suggesting that the capillary pressure gradient in the streamwise direction is negligible compared to that in the cross-stream direction.

The film evolution equation resulting from the model is (full derivation in the Appendix):

$$U_b \frac{\partial h}{\partial z} - \frac{\sigma}{3\mu} \nabla \cdot \left[h^3 \nabla \left(\nabla^2 h \right) \right] = 0 \tag{13}$$

Using the observation that the capillary pressure gradient in the streamwise direction is negligible compared to that in the cross-stream direction, the equation above simplifies into:

$$U_b \frac{\partial h}{\partial z} - \frac{\sigma}{3\mu} \frac{\partial}{\partial x} \left(h^3 \frac{\partial^3 h}{\partial x^3} \right) = 0 \tag{14}$$

Equation (14) is essentially a continuity equation for the volumetric flow of liquid in the film per unit area. It demonstrates that streamwise changes of the liquid film thickness, $\partial h/\partial z$, occur as a result of the transversal flows triggered by the cross-stream capillary pressure gradient, which originates from changes in the interface curvature. Equation (14) can be made nondimensional by defining a new set of variables:

$$Z = \frac{1}{3\mathrm{Ca_b}} \frac{h_0^3}{R_h^4} (z_N - z), \quad X = \frac{x}{R_h}, \quad H = \frac{h}{h_0} \tag{15}$$

where h_0 is a reference film thickness value, e.g. the initial minimum film thickness where the dimple first appears in the vicinity of the bubble nose.

Replacing these variables into Eq. (14) removes all parameters:

$$\frac{\partial H}{\partial Z} + \frac{\partial}{\partial X}\left(H^3 \frac{\partial^3 H}{\partial X^3}\right) = 0 \tag{16}$$

Equation (16) not only describes the evolution of the liquid film trapped between long bubbles and polygonal channels, but it has also been applied to study the pinching of soap films [43], the film drainage in droplet coalescence [44] and the capillary drainage of annular films [45, 46]. Numerical and semi-analytical solutions of Eq. (16) are available in the literature [40, 43, 44, 45, 46], and show that the film thins by forming a localised dimple where, at sufficiently large values of Z, the thickness decreases as $H_{min} \sim Z^{-0.5}$, i.e. $h_{min} \sim (z_N - z)^{-0.5}$ in the dimensional coordinates adopted in this work. The exponent 0.5 agrees remarkably well with the present simulation results reported in Fig. 8, in particular in the low capillary number range, $\mathrm{Ca_l} < 0.005$. As $\mathrm{Ca_l} > 0.005$, the data in Fig. 8 show an increasing deviation of β from the asymptotic value 0.5, with the film that thins more rapidly as $\mathrm{Ca_l}$ is increased. A possible explanation for this discrepancy is that as $\mathrm{Ca_l}$, and thus $\mathrm{Ca_b}$, increase, the nondimensional coordinate Z decreases (see Eq. (15)) and therefore the asymptotic solution is achieved at much larger distances from the bubble nose.

4.2. Flows with inertia

In this section, we study the effect of inertial forces on the bubble and thin-film dynamics. For five selected values of the liquid capillary number, we vary the Reynolds number in the range $\mathrm{Re_l} = 1 - 2000$, with the resulting Weber number reaching values as high as $\mathrm{We_l} = 50$. For flows in circular channels, the Reynolds number has a mixed effect on the thickness of the

flat film region. Until intermediate values, $\mathrm{Re_l} \leq 100 - 500$, the liquid film exhibits a thinning trend, whereas at larger $\mathrm{Re_l}$ the film thickness increases monotonically [34]. Also, the bubble nose elongates for increasing Reynolds numbers [12], and hence it takes a longer bubble in order for a flat film region to form.

Representative cross-sectional profiles of the bubble for increasing $\mathrm{Re_l}$, at fixed $\mathrm{Ca_l} = 0.005$, are presented in Fig. 10(a). As $\mathrm{Re_l}$ is increased, the film thickness at the channel centre decreases and converges to the minimum film thickness value, such that the dimple becomes barely visible when $\mathrm{Re_l} = 2000$. The reduced curvature of the dimple observed in Fig. 10(a) as $\mathrm{Re_l}$ is increased, is a consequence of plotting the interface profile at a fixed distance from the bubble nose. We observe that inertia retards the formation of the dimple, from a distance of about $1R_h$ behind the bubble nose when $\mathrm{Re_l} = 10$, to about $9R_h$ when $\mathrm{Re_l} = 2000$, and that the dimple shifts towards the channel centre as $\mathrm{Re_l}$ is increased; see the additional data included in the Supplementary Material. The corresponding minimum film thickness streamwise profiles are depicted in Fig. 10(b). As $\mathrm{Re_l}$ increases, the zone identified as the bubble nose in Fig. 8 becomes much longer, thus retarding the formation of the interface dimple. The exponentially-thinning film zone still appears once the dimple has formed, although farther from the nose. The slope of the minimum thickness profile in this zone, extracted as exponent of the power-law $h_{min} \sim (z_N - z)^{-\beta}$, increases from $\beta = 0.56$ at $\mathrm{Re_l} = 10$ to $\beta = 0.77$ at $\mathrm{Re_l} = 2000$, and thus the film thins at a faster rate in the presence of inertial effects. Therefore, sufficiently far from the bubble nose, the minimum film thickness reduces monotonically with an increase of the

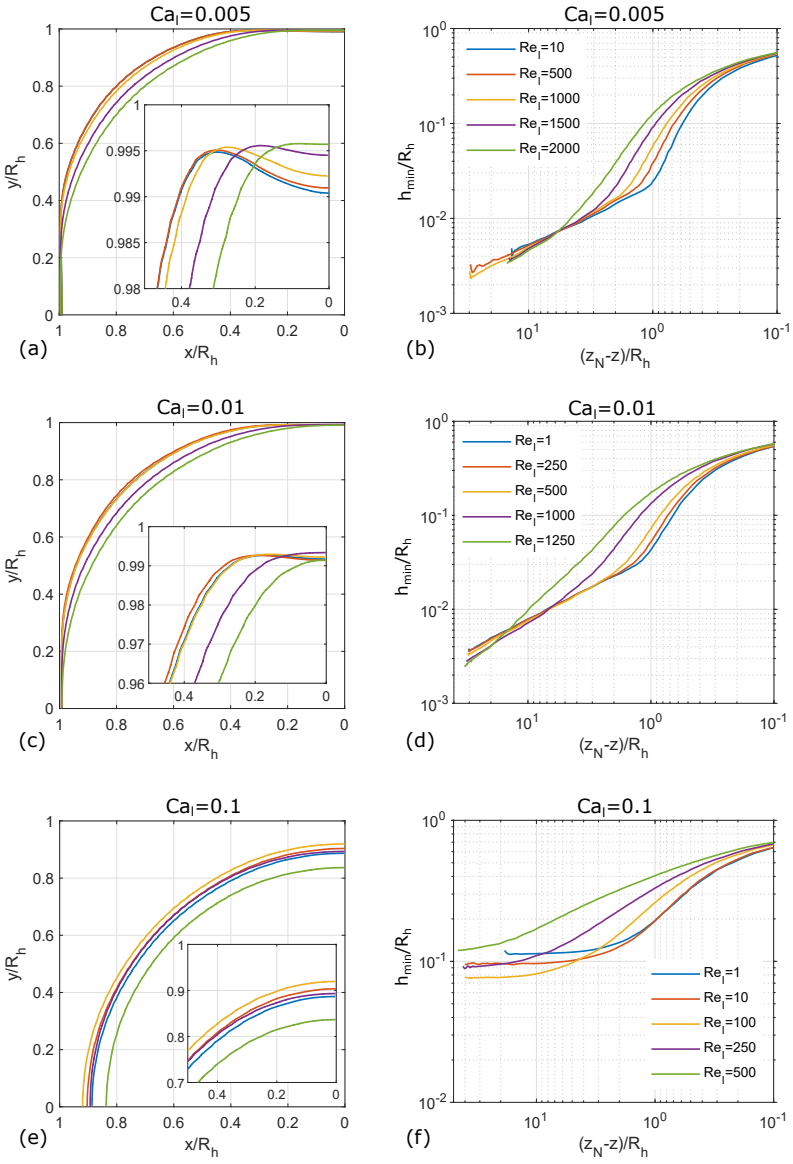

Figure 10: (a,c,e) Cross-sectional liquid-gas interface profiles extracted $11R_h$ behind the bubble nose, and (b,d,f) streamwise profiles of the minimum film thickness for selected capillary and Reynolds numbers.

Reynolds number.

Similar trends are detected when varying $\mathrm{Re_l}$ at fixed $\mathrm{Ca_l} = 0.01$. Figure 10(c) shows that, at $11R_h$ behind the bubble nose, the dimple has not yet formed when $\mathrm{Re_l} \geq 1000$. We observe that it takes about $14R_h$ for it to form when $\mathrm{Re_l} = 1000$ (see data in the Supplementary Material), while for $\mathrm{Re_l} = 1250$ the dimple is never formed, even for a bubble that is about $30R_h$ long. The slope of the exponentially-thinning film zone, see Fig. 10(d), increases with $\mathrm{Re_l}$, from $\beta = 0.67$ at $\mathrm{Re_l} = 10$ to $\beta = 0.81$ at $\mathrm{Re_l} = 1000$, whereas the bubble is not long enough for it to develop when $\mathrm{Re_l} = 1250$. At long distance from the bubble nose, $z_N - z > 30R_h$, h_{min} decreases monotonically with the increase of $\mathrm{Re_l}$.

When $\mathrm{Ca_l} = 0.1$, see Fig. 10(e) and (f), the bubble is axisymmetric for all the values of $\mathrm{Re_l}$ tested. For $\mathrm{Re_l} \leq 100$, the bubble length is always sufficient in order for a flat film region to appear along the bubble body. In this range, the thickness of the flat film decrases when increasing $\mathrm{Re_l}$, similarly to flows in circular capillaries. For $\mathrm{Re_l} \geq 250$, a bubble length of $40R_h$ is not sufficient for a flat film region to develop due to the extreme elongation of the nose. However, extrapolation of the purple ($\mathrm{Re_l} = 250$) and green ($\mathrm{Re_l} = 500$) profiles in Fig. 10(f) to longer bubbles suggest that the trend of film thickness with $\mathrm{Re_l}$ is reversed, i.e. the thickness increases with $\mathrm{Re_l}$.

The results for all the simulations run with inertial effects are compiled in Fig. 11, where minimum film thicknesses and gas area fractions are measured on a cross-section $11R_h$ behind the bubble nose. For $\mathrm{Ca_l} = 0.005, 0.01$, the minimum thickness decreases when increasing $\mathrm{Re_l}$, because the bubble nose, where the film exhibits the steeper thinning rate, becomes longer, and

because the slope of the exponentially-thinning film zone becomes steeper. The reversed trend observed for $\mathrm{Ca_l} = 0.01$ and $\mathrm{Re_l} > 1000$ is exclusively a consequence of fixing the measurement section at $11R_h$, whereas it takes a longer distance for the bubble nose to develop. For cylindrical bubbles, $\mathrm{Ca_l} \geq 0.05$, the film thickness trends with $\mathrm{Re_l}$ are in agreement with those for circular channels. The bubble speed, reported in Fig. 11(b), exhibits a slight decrease with increasing $\mathrm{Re_l}$ at low-intermediate values of $\mathrm{Re_l}$, while it increases steeply at large Reynolds numbers. The values of gas area fraction (Fig. 11(c)) are related to the velocity ratio via Eq. (9). For $\mathrm{Re_l} \leq 100$, area fractions do not differ appreciably from the values measured in the visco-capillary regime ($\mathrm{We} \ll 1$), whereas at large Reynolds numbers the reduction of the gas area fraction owing to increased inertial effects is remarkable.

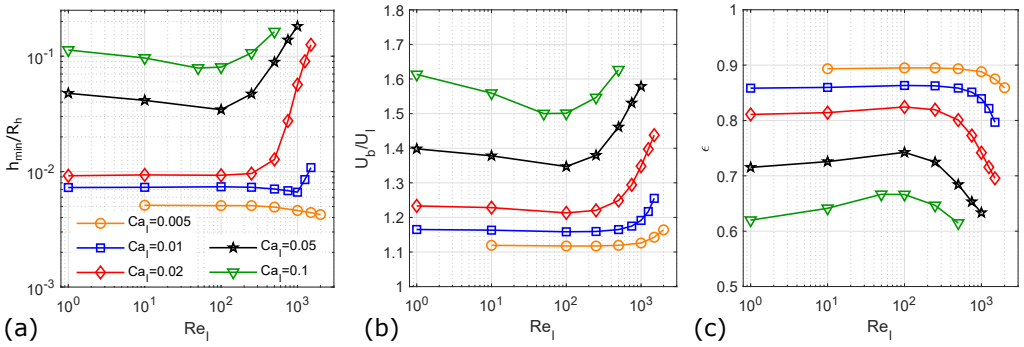

Figure 11: Effect of capillary and Reynolds numbers on the (a) minimum film thickness, (b) bubble-to-liquid velocity ratio and (c) gas area fraction. Film thickness and gas area fraction are measured on a cross-section located $11R_h$ behind the tip of the bubble nose.

5. Conclusions

We have performed a systematic analysis of the topology of long gas bubbles travelling within square capillaries. We have investigated both the visco-capillary and visco-inertial regimes, by varying the capillary and Reynolds numbers of the flow in the range $\mathrm{Ca_l} = 0.002 - 0.5$ and $\mathrm{Re_l} = 1 - 2000$. The study is based on the results of direct numerical simulations conducted utilising the Volume-Of-Fluid method implemented in the solver interFoam of OpenFOAM. This study emphasises the fact that the dynamics of elongated bubbles in square channels, and the thickness of the resulting liquid films, differ substantially from those reported for circular channels. The main conclusions of this work are as follows:

- Bubbles have unique topological features depending on the capillary number. When $\mathrm{Ca_b} \geq 0.05$, the bubbles are cylindrical and a flat film region develops, provided that the bubble is sufficiently long. When $0.01 < \mathrm{Ca_b} < 0.05$, the confinement effect of the channel walls flattens the liquid-gas interface at the channel centre, and the bubble cross-section is no longer axisymmetric. When $\mathrm{Ca_b} \leq 0.01$, the thin film at the channel centre exhibits a saddle shape, and an interfacial dimple is formed at the matching point between the thin-film at the centre and the thick menisci at the corners.

- The centreline and minimum liquid film thicknesses in square channels are up to one order of magnitude smaller than that reported for bubbles travelling in circular tubes. The scaling law $h_{min} \sim \mathrm{Ca_b}^1$ applies as $\mathrm{Ca_b} \to 0$, in agreement with the available theory, in contrast with the

law $h \sim \mathrm{Ca_b}^{2/3}$ for circular channels.

- The interfacial dimple, where the film exhibits a minimum thickness, appears at a constant distance from the channel centre, and this distance varies with $\mathrm{Ca_l}$ and $\mathrm{Re_l}$. Dewetting of the film is likely to initiate at this location.

- Unlike flow in circular channels, a flat film region is never achieved along the bubble at small capillary numbers, and thus the bubble length impacts considerably the film thickness magnitude. The film thins as an exponential function of the distance from the nose, $h_{min} \sim (z_N - z)^{-\beta}$, with β converging to the asymptotic value of 0.5 as $\mathrm{Ca_l}$ decreases, in the inertialess regime.

- Inertial effects retard the formation of the interfacial dimple, which may never form if the bubble is not sufficiently long. However, the film thins at a faster rate towards the bubble rear as $\mathrm{Re_l}$ is increased.

- The trend of the film thickness with $\mathrm{Re_l}$ is mixed, as this depends also on $\mathrm{Ca_l}$ and on the bubble length. The gas area fraction exhibits a marked dependence on $\mathrm{Re_l}$ when inertial forces become dominant.

Acknowledgements

O. K. M. acknowledges funding from PETRONAS and the Royal Academy of Engineering for Research Chair.

Supplementary material

Supplementary material associated with this article is included with the submission. This provides a comparison with the experimental data of Marschall et al. [33], and additional data about the shape of long bubbles for flows with inertial effects.

Appendix A. Equations governing the flow in the thin-film region at the channel centre

In the thin-film region bounded between the bubble interface and the wall at the channel centre, the liquid-gas interface is nearly parallel to the wall ($|\nabla h| \ll 1$) and the velocity field can be described as a two-component vector $\mathbf{u}(x, y, z) = u(x, y, z)\mathbf{i} + w(x, y, z)\mathbf{k}$. The continuity equation reads as follows:

$$\frac{\partial u}{\partial x} + \frac{\partial w}{\partial z} = 0 \tag{A.1}$$

Under the lubrication approximation, the x and z components of the momentum equation can be written in compact notation as:

$$\nabla p = \mu \frac{\partial^2 \mathbf{u}}{\partial y^2} \tag{A.2}$$

where $\nabla = \mathbf{i}\,\partial/\partial x + \mathbf{k}\,\partial/\partial z$ and $p = p(x, y, z)$, and along y:

$$\frac{\partial p}{\partial y} = 0 \tag{A.3}$$

which means that the pressure is constant along y, $p = p(x, z)$. We adopt a reference frame moving with the bubble at a speed $U_b\mathbf{k}$. Therefore, at the channel wall, $y = R_h$, the no-slip condition requires that:

$$\mathbf{u} = -U_b\mathbf{k} \tag{A.4}$$

At the liquid-gas interface, $y = R_h - h(x,z)$, the stress jump conditions at leading-order write as [16]:

$$\frac{\partial \mathbf{u}}{\partial y} = 0 \tag{A.5}$$

and:

$$p - p_b = \sigma\kappa = -\sigma\nabla^2 h \tag{A.6}$$

where p_b is the pressure within the bubble, assumed constant. $\kappa(x,z)$ is the local curvature of the interface, that under the small-slope assumption ($|\nabla h| \ll 1$) is expressed as $\kappa = -\nabla^2 h$. The integration of Eq. (A.3), with the integration constant set by Eq. (A.6), provides an expression for the pressure field in the liquid film:

$$p(x,z) = p_b - \sigma\nabla^2 h(x,z) \tag{A.7}$$

and for the pressure gradient:

$$\nabla p = -\sigma\nabla\left(\nabla^2 h\right) \tag{A.8}$$

Equations (A.7) and (A.8) coincide, respectively, with Eqs. (10) and (11) in the article. Integration of Eq. (A.2) along y, with the boundary conditions in Eqs. (A.4) and (A.5), yields the velocity profile in the liquid film:

$$\mathbf{u}(x,y,z) = -U_b\mathbf{k} + \frac{1}{\mu}\nabla p\left[\frac{1}{2}(R_h - y)^2 - h(R_h - y)\right] \tag{A.9}$$

which is Eq. (12) in the article. A volumetric flow rate $\mathbf{q}(x,z)$ is identified by integrating the velocity profile given by Eq. (A.9) across the film:

$$\mathbf{q} = \int_{R_h - h}^{R_h} \mathbf{u}\, dy = -U_b h\mathbf{k} - \frac{h^3}{3\mu}\nabla p \tag{A.10}$$

which represents the volumetric flow of liquid across a plane area normal to $\mathbf{u}$, with unit width and with height equal to the film thickness. The divergence of the volumetric flow rate can be written as a function of the velocity derivatives as:

$$\nabla \cdot \mathbf{q} = \frac{\partial q_x}{\partial x} + \frac{\partial q_z}{\partial z} = \frac{\partial}{\partial x} \int_{R_h - h}^{R_h} u \, dy + \frac{\partial}{\partial z} \int_{R_h - h}^{R_h} w \, dy \tag{A.11}$$

and, using the chain rule:

$$\begin{aligned} &\frac{\partial}{\partial x} \int_{R_h - h}^{R_h} u \, dy + \frac{\partial}{\partial z} \int_{R_h - h}^{R_h} w \, dy = \\ &= \int_{R_h - h}^{R_h} \frac{\partial u}{\partial x} \, dy + u(x, R_h - h, z) \frac{\partial h}{\partial x} + \int_{R_h - h}^{R_h} \frac{\partial w}{\partial z} \, dy + w(x, R_h - h, z) \frac{\partial h}{\partial z} \end{aligned} \tag{A.12}$$

Owing to the small-slope assumption, $|\nabla h| \ll 1$, the second and fourth terms at the right-hand side of Eq. (A.12) are negligible, thus it follows that:

$$\nabla \cdot \mathbf{q} = \int_{R_h - h}^{R_h} \frac{\partial u}{\partial x} \, dy + \int_{R_h - h}^{R_h} \frac{\partial w}{\partial z} \, dy \tag{A.13}$$

and, since the right-hand side of Eq. (A.13) coincides with the continuity equation, integrated along y across the film, this must be zero:

$$\nabla \cdot \mathbf{q} = 0 \tag{A.14}$$

Introducing Eq. (A.10) into Eq. (A.14) yields:

$$U_b \frac{\partial h}{\partial z} + \frac{1}{3\mu} \nabla \cdot \left(h^3 \nabla p \right) = 0 \tag{A.15}$$

and, using Eq. (A.8) to rewrite the capillary pressure gradient, we obtain:

$$U_b \frac{\partial h}{\partial z} - \frac{\sigma}{3\mu} \nabla \cdot \left[h^3 \nabla \left(\nabla^2 h \right) \right] = 0 \tag{A.16}$$

which is the differential equation describing the evolution of the film thickness $h(x, z)$ in the thin-film region at the channel centre [42, 16, 34], Eq. (13) in the article.

References

[1] T. G. Karayiannis, M. M. Mahmoud, Flow boiling in microchannels: Fundamentals and applications, Appl. Therm. Eng. 115 (2017) 1372 – 1397.

[2] Q. Zhang, S. M. Hassanizadeh, B. Liu, J. F. Schijven, N. K. Karadimitriou, Effect of hydrophobicity on colloid transport during two-phase flow in a micromodel, Water Resour. Res. 50 (2014) 7677–7691.

[3] S. Khodaparast, M. K. Kim, J. Silpe, H. A. Stone, Bubble-driven detachment of bacteria from confined micro-geometries, Environ. Sci. Technol. 51 (2017) 1340–1347.

[4] Y. Hu, S. Bian, J. Grotberg, M. Filoche, J. White, S. Takayama, J. B. Grotberg, A microfluidic model to study fluid dynamics of mucus plug rupture in small lung airways, Biomicrofluidics 9 (2015) 044119.

[5] M. A. Safi, N. I. Prasianakis, J. Mantzaras, A. Lamibrac, F. B. Büchi, Experimental and pore-level numerical investigation of water evaporation in gas diffusion layers of polymer electrolyte fuel cells, Int. J. Heat Mass Tran. 115 (2017) 238 – 249.

[6] A. de Lózar, A. L. Hazel, M. Heil, Scaling properties of coating flows in rectangular channels, Phys. Rev. Lett. 99 (2007) 234501.

[7] F. P. Bretherton, The motion of long bubbles in tubes, J. Fluid Mech. 10 (1961) 166–188.

[8] G. I. Taylor, Deposition of a viscous fluid on the wall of a tube, J. Fluid Mech. 10 (1960) 161–165.

[9] P. Aussillous, D. Quéré, Quick deposition of a fluid on the wall of a tube, Phys. Fluids 12 (2000) 2367–2371.

[10] Y. Han, N. Shikazono, Measurement of the liquid film thickness in microtube slug flow, Int. J. Heat Fluid Flow 30 (2009) 842–853.

[11] A. de Ryck, The effect of weak inertia on the emptying of a tube, Phys. Fluids 14 (2002) 2102–2108.

[12] M. Magnini, A. Ferrari, J. R. Thome, H. A. Stone, Undulations on the surface of elongated bubbles in confined gas-liquid flows, Phys. Rev. Fluids 2 (2017) 084001.

[13] J. Ratulowski, H.-C. Chang, Transport of gas bubbles in capillaries, Phys. Fluids A 1 (1989) 1642–1655.

[14] W. B. Kolb, R. L. Cerro, Coating the inside of a capillary of square cross-section, Chem. Eng. Sci. 46 (1991) 2181–2195.

[15] W. B. Kolb, R. L. Cerro, The motion of long bubbles in tubes of square cross-section, Phys. Fluids A 5 (1993) 1549–1557.

[16] H. Wong, C. J. Radke, S. Morris, The motion of long bubbles in polygonal capillaries. Part 1. Thin films, J. Fluid Mech. 292 (1995) 71–94.

[17] H. Wong, C. J. Radke, S. Morris, The motion of long bubbles in polygonal capillaries. Part 2. Drag, fluid pressure and fluid flow, J. Fluid Mech. 292 (1995) 95–110.

[18] A. L. Hazel, M. Heil, The steady propagation of a semi-infinite bubble into a tube of elliptical or rectangular cross-section, J. Fluid Mech. 470 (2002) 91–114.

[19] A. de Lózar, A. Juel, A. L. Hazel, The steady propagation of an air finger into a rectangular tube, J. Fluid Mech. 614 (2008) 173–195.

[20] H. Chen, Q. Meng, J. Li, Thin lubrication film around moving bubbles measured in square channels, Appl. Phys. Lett. 107 (2015) 141608.

[21] H. Chen, Z. Li, J. Li, Thin-film profile around long bubbles in square microchannels measured by chromatic interference method, Appl. Phys. Lett. 109 (2016) 041604.

[22] S. Khodaparast, O. Atasi, A. Deblais, B. Scheid, H. A. Stone, Dewetting of thin liquid films surrounding long bubbles in microchannels, Langmuir 34 (2018) 1363–1370.

[23] C. W. Hirt, B. D. Nichols, Volume of fluid (VOF) method for the dynamics of free boundaries, J. Comput. Phys. 39 (1981) 201–225.

[24] J. U. Brackbill, D. B. Kothe, C. Zemach, A continuum method for modeling surface tension, J. Comput. Phys. 100 (1992) 335–354.

[25] H. G. Weller, A new approach to VOF-based interface capturing methods for incompressible and compressible flows, OpenCFD Ltd. Report TR/HGW/04 (2008).

[26] S. S. Deshpande, L. Anumolu, M. F. Trujillo, Evaluating the performance of the two-phase flow solver interFoam, Comput. Sci. Discov. 5 (2012) 1–36.

[27] A. Ferrari, M. Magnini, J. R. Thome, A Flexible Coupled Level Set and Volume of Fluid (flexCLV) method to simulate microscale two-phase flow in non-uniform and unstructured meshes, Int. J. Multiph. Flow 91 (2017) 276–295.

[28] S. Khodaparast, M. Magnini, N. Borhani, J. R. Thome, Dynamics of isolated confined air bubbles in liquid flows through circular microchannels: an experimental and numerical study, Microfluid Nanofluid 19 (2015) 209–234.

[29] B. van Leer, Towards the ultimate conservative difference scheme. V. A second-order sequel to Godunov's method, J. Comput. Phys. 32 (1979) 101–136.

[30] R. I. Issa, Solution of the implicitly discretized fluid flow equations by operator-splitting, J. Comput. Phys. 62 (1985) 40–65.

[31] R. Gupta, D. F. Fletcher, B. S. Haynes, On the CFD modelling of Taylor flow in microchannels, Chem. Eng. Sci 64 (2009) 2941–2950.

[32] M. Magnini, B. Pulvirenti, J. R. Thome, Numerical investigation of hydrodynamics and heat transfer of elongated bubbles during flow boiling in a microchannel, Int. J. Heat Mass Tran. 59 (2013) 451–471.

[33] H. Marschall, S. Boden, C. Lehrenfeld, C. J. Falconi, U. Hampel, R. A., M. Worner, D. Bothe, Validation of Interface Capturing and Tracking techniques with different surface tension treatments against a Taylor bubble benchmark problem, Comput. Fluids 102 (2014) 336–352.

[34] M. T. Kreutzer, F. Kapteijn, J. A. Moulijn, C. R. Kleijn, J. J. Heiszwolf, Inertial and interfacial effects on pressure drop of Taylor flow in capillaries, AIChE J. 51 (2005) 2428–2440.

[35] Y. Han, N. Shikazono, Measurement of liquid film thickness in micro square channel, Int. J. Multiph. Flow 35 (2009) 896–903.

[36] M. T. Kreutzer, F. Kapteijn, J. A. Moulijn, J. J. Heiszwolf, Multiphase monolith reactors: Chemical reaction engineering of segmented flow in microchannels, Chem. Eng. Sci. 60 (2005) 5895–5916.

[37] A. Ferrari, M. Magnini, J. R. Thome, Numerical analysis of slug flow boiling in square microchannels, Int. J. Heat Mass Tran. 123 (2018) 928–944.

[38] T. C. Thulasidas, M. A. Abraham, R. L. Cerro, Bubble-train flow in capillaries of circular and square cross-section, Chem. Eng. Sci 50 (1995) 183–199.

[39] M. Magnini, S. Khodaparast, O. K. Matar, J. R. Thome, H. A. Stone,

Dynamics of long gas bubbles rising in a vertical tube in a cocurrent liquid flow, Phys. Rev. Fluids 4 (2019) 023601.

[40] M. T. Kreutzer, M. S. Shah, P. Parthiban, S. A. Khan, Evolution of non-conformal Landau-Levich-Bretherton films of partially wetting liquids, Phys. Rev. Fluids 3 (2018) 014203.

[41] M. Magnini, O. K. Matar, Numerical study of the impact of the channel shape on microchannel boiling heat transfer, Int. J. Heat Mass Tran. 150 (2020) 119322.

[42] A. Oron, S. H. Davis, S. G. Bankoff, Long-scale evolution of thin liquid films, Rev. Mod. Phys. 69 (1997) 931–980.

[43] A. Aradian, E. Raphael, P. G. de Gennes, Marginal pinching in soap films, Europhys. Lett. 55 (2001) 834–840.

[44] A. F. Jones, S. D. R. Wilson, The film drainage problem in droplet coalescence, J. Fluid Mech. 87 (1978) 263–288.

[45] P. S. Hammond, Nonlinear adjustment of a thin annular film of viscous fluid surrounding a thread of another within a circular cylindrical pipe, J. Fluid Mech. 137 (1983) 363–384.

[46] J. R. Lister, J. M. Rallison, A. A. King, L. J. Cummings, O. E. Jensen, Capillary drainage of an annular film: the dynamics of collars and lobes, J. Fluid Mech. 552 (2006) 311–343.